# The *HST*/ACS Grism Parallel Survey: II. First Results and a Catalog of Faint Emission-Line Galaxies at $z \leq 1.6$

Igor Drozdovsky[1,2], Lin Yan[1], Hsiao-Wen Chen[3], Daniel Stern[4], Robert Kennicutt, Jr.[5], Hyron Spinrad[6], & Steve Dawson[6]

## ABSTRACT

We present the first results from the *Hubble Space Telescope* (*HST*) Advanced Camera for Surveys (ACS) Grism Parallel Survey, a large program obtaining deep, slitless ACS grism spectroscopy of high-latitude *HST* parallel fields. We report on 11 high Galactic latitude fields here, each with grism integration times $> 12$ ks. We identify 601 compact emission line galaxies at $z \leq 1.6$, reaching emission lines to a flux limit of $\gtrsim 5 \times 10^{-18}$ ergs cm$^{-2}$ s$^{-1}$ ($3\sigma$). We determine redshifts by cross correlation of the target spectra with template spectra, followed by visual inspection. We measure star formation rates from the observed [O II] $\lambda$3727, [O III] $\lambda$5007, and H$\alpha$ line fluxes. Follow-up observations with the Keck telescope of one of the survey fields confirms our classification and redshifts with $\sigma(z) \simeq 0.02$. This is one of the deepest emission line surveys to date, covering a total area of 121 arcmin$^2$. The rough estimate of the co-moving number density of emission-line galaxies in our survey at $0.3 < z < 1.3$ is $\sim 4.5 \times 10^{-3}\, h_{70}^{-3}$ Mpc$^{-3}$. We reach deeper into the emission-line luminosity function than either the STIS or NICMOS grism parallel surveys, finding an apparent space density of emission line galaxies several times higher than those surveys. Because of the ACS high spatial resolution, our survey is very sensitive to faint, compact galaxies with strong emission lines and weak continua. The ACS grism survey provides the co-moving star formation density at $z \leq 1.6$ at a high level of completeness.

*Subject headings:* galaxies: catalogs — galaxies: high redshift — surveys

## 1. Introduction

One of the key unanswered questions of modern cosmology is the origin and extent of the decline in the star formation rate of the Universe between $z \sim 1.5$ and the present epoch (e.g., Gallego et al. 1995; Tresse & Maddox 1998; Lilly et al. 1996; Cowie et al. 1999; Hippelein et al. 2003). Based on studies of star-forming and evolving galaxies as a function of look-back time, a picture has emerged in which more massive galaxies undergo a larger fraction of their star formation at earlier times than less massive ones (e.g., Cowie et al. 1996; Gavazzi & Scodeggio 1996; Cimatti et al. 2004; Glazebrook et al. 2004; Kodama et al. 2004). This potentially presents a challenge for existing models of galaxy formation (e.g., Brinchmann et al. 2004). To fully address this question, it is necessary to obtain a comprehensive sample of star-forming galaxies of different masses and morphological types at a broad range of redshifts; deep spectroscopic surveys provide ideal samples for this endeavor.

The low sky background and high spatial resolution afforded by space makes emission line surveys from above the atmosphere particularly sensitive and powerful tools for studying galaxy for-

[1] *Spitzer* Science Center, California Institute of Technology, MS 100-22, Pasadena, CA 91125

[2] Astronomical Institute of St.Petersburg University, Petrodvoretz, 198504, Russia

[3] Massachusetts Institute of Technology, Cambridge, MA 02138

[4] Jet Propulsion Laboratory, California Institute of Technology, Mail Stop 169-506, Pasadena, CA 91109

[5] Steward Observatory, University of Arizona, 933 N. Cherry Ave., Tucson, AZ 85721

[6] Department of Astronomy, 601 Campbell Hall, University of California, Berkeley, CA 94720

mation and evolution. Ground-based, objective-prism programs, such as the Kitt Peak International Spectroscopic Survey (KISS; Gronwall et al. 2004) have been quite effective at identifying bright, low-redshift H$\alpha$ emitters over wide areas of sky. To date, KISS has identified 2266 emission-line objects over 182 deg$^2$, to a limiting flux of $1\times10^{-15}$ ergs cm$^{-2}$ s$^{-1}$. Ground-based surveys have also been effective at identifying faint, high-redshift Ly$\alpha$ emitters in gaps between the telluric night-sky lines (e.g., Hu et al. 1998; Rhoads et al. 2000; Kodaira et al. 2003; Stern et al. 2005), reaching typical limiting line fluxes of $\approx 2\times10^{-17}$ ergs cm$^{-2}$ s$^{-1}$. Slitless, grism surveys from space provide the opportunity to identify fainter lines unobstructed by telluric OH emission. Furthermore, parallel programs with the *Hubble Space Telescope* (*HST*) provide, at no cost to the observatory efficiency, surveys which are less susceptible than pencil beam surveys to the bias induced by cosmic variance (e.g., Cohen et al. 2000).

Previous *HST* parallel slitless spectroscopic programs with the Space Telescope Imaging Spectrometer (STIS; Gardner et al. 1998; Teplitz et al. 2003) and the Near-Infrared Camera and Multi-Object Spectrograph (NICMOS; McCarthy et al. 1999; Yan et al. 1999) have left a valuable scientific legacy studying faint emission line galaxies out to high redshift. In particular, the lack of telluric emission lines allowed the NICMOS Parallel Survey to identify an impressive census of high-redshift galaxies whose optical features are shifted into the near-infrared. ACS, though observing at the same wavelength regime as STIS, provides higher spatial resolution data and is a factor of a few more sensitive to emission lines, thus providing a significant increase in our ability to study faint emission-line galaxies (Pirzkal et al. 2004).

In this paper we present the analysis of eleven deep spectroscopic fields from the ACS parallel survey. ACS slitless spectra provide unprecedented sensitivity in the range $5500 < \lambda < 10500$ Å, where ground-based spectroscopy is challenged by the night sky. We discuss a sample of $z \leq 1.6$ galaxies selected by the presence of [O II] $\lambda$3727, [O III] $\lambda$5007 and/or H$\alpha$ emission features. Our survey is well-suited for exploring the faint end of the star-forming galaxy luminosity function, identifying Ly$\alpha$ emitting galaxies at $4 \lesssim z \lesssim 7$, and for studying the spatially-resolved star formation rate in individual galaxies. This paper presents the first results from our survey. In §2 we describe our observation and data reduction methodologies. In §3 we describe how redshifts are determined and present a comparison of our ACS grism redshifts to ground-based observations obtained at Keck Observatory. In §4 we present initial results from our survey, including measurements of star formation rates for individual galaxies (§4.2) and ACS morphologies of actively star-forming galaxies (§4.3). Our results are summarized in §5. The first paper in this series describes our data reduction scheme in detail (Paper I; Chen et al. 2005); future papers will address the faint end of the luminosity function for star-forming galaxies (Paper III; Drozdovsky et al., in preparation), and the early-type galaxy sample at $0.6 \lesssim z \lesssim 1.3$ detected with the grism spectra (Paper IV; Yan et al., in preparation).

Throughout this paper, unless otherwise specified, magnitudes refer to the Vega system and we adopt a flat, $\Lambda$-dominated universe ($H_0 = 70\,h_{70}$ km s$^{-1}$ Mpc$^{-1}$, $\Omega_M = 0.3$, $\Omega_\Lambda = 0.7$).

## 2. *HST*/ACS Observations

All *HST* data presented here were obtained with the Wide Field Camera (WFC) on ACS. The observing program was designed to acquire a pair of images at each pointing: a direct image taken with a broad-band filter (typically F775W or F814W) and a dispersed image taken with the G800L grism (see Table 1). The direct images are important both for registering the grism frames to a common origin and for the $0^{\rm th}$ order wavelength calibration of the grism spectra. The WFC/G800L grism has a mean dispersion of $\sim 40$ Å pix$^{-1}$ in the first order (Pavlovsky 2004). The actual, observed resolution is a function of the apparent image size convolved with the WFC point spread function (PSF). From the observations described herein, the realized spectral resolution, $R_\lambda$, is $\sim 80$ to $\sim 150$. Small variations in the PSF due to changes in the optical telescope assembly (cf., *breathing*) and longer term changes in the internal structure of ACS introduce small variations in the maximal achievable resolution.

### 2.1. Parallel observing mode and scheduling

Approximately half of the observations for this investigation were obtained with *HST* operating in parallel mode as part of GO/PAR program 9468[1] (P.I. Lin Yan). While this allowed us to collect far more data than would be possible in a single primary program, it limited our ability to plan and execute the observations in a manner that optimized the scientific return. Since July 2002, the ACS/WFC parallels were scheduled during much of the time for which NICMOS or STIS were the primary instruments. The observing algorithm for this program was quite simple. In each full orbit one of the following exposure sequences was selected: F606W and/or F814W imaging followed by G800L grism observations with exposure times of approximately 500 s. The preferred ratio of exposure times was F814W:F606W:G800L = 1:1:3. The selection of the exposure sequence for any given orbit was nearly random, but was weighted in favor of the spectroscopy. The dither step and orientation depended upon the primary observing programs, and we preferentially use programs with fixed orientation and small dither offsets.

Another half of our data were obtained from the *HST* Archive as part of guest observer parallel GO/PAR program 9482 (P.I. James Rhoads), and data for the J 08:08+06:43 field are from GO program 9405 (P.I. Andy Fruchter). The basic observing approaches were similar to ours, though with alternate filter selections (see Table 1).

During the period from July 2002 to October 2003, approximately 800 ACS grism exposures (roughly 200 orbits) were observed. These were distributed in $\sim 40$ independent pointings with integration time of each individual grism exposure ranging from 300 s to 1200 s. Rather than adopt a strict latitude cutoff we chose to reduce all of the data and reject those with high stellar densities. Depth of the grism images is the major limitation of the study. For this study we choose 11 fields with total grism exposure time more than $> 12$ ks, covering about 121 square arcminutes.

The final depth achieved varied from field to field. We define our limiting depths as $3\sigma$ within a 4 pixel aperture. This aperture reasonably represents the area of the ACS/WFC PSF. Fig. 1 shows an area-depth histogram for our survey. Our median limiting depth is $\sim 1.6 \times 10^{-17}$ ergs cm$^{-2}$ s$^{-1}$ and our deepest three fields reach a depth of $\sim 5 \times 10^{-18}$ ergs cm$^{-2}$ s$^{-1}$, which is approximately a factor of two deeper than typical ground-based narrow-band/spectroscopic surveys and 2−5 times deeper than the HST/NICMOS (McCarthy et al. 1999; Yan et al. 1999) and STIS (Teplitz et al. 2003) parallel surveys.

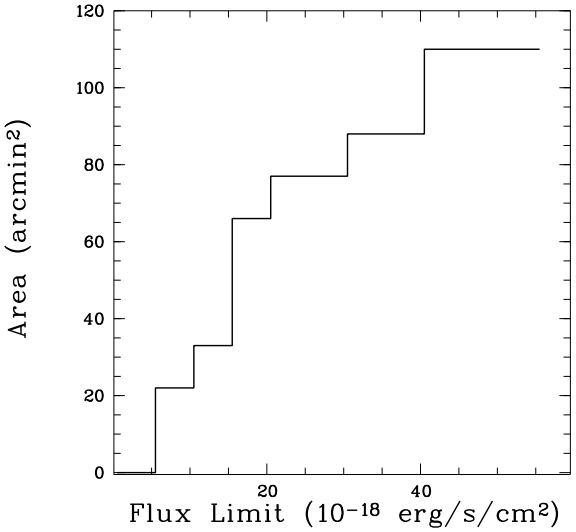

Fig. 1.— Area-depth histogram for the ten ACS grism parallel fields discussed here. Flux limits refer to $3\sigma$ limits in 4 pix apertures; this aperture reasonably represents the ACS/WFC PSF.

### 2.2. Data processing and analysis

The extraction of the spectra from the grism images is a multi-stage process. The main steps of the reduction procedure are: standard `CALACS` pipeline reduction (e.g., bias subtraction); cosmic ray detection and global sky background removal; combining the 2D images; generating object catalogs from the direct images; extraction and calibration of 1D spectra from the coadded grism images; combination of the 1D spectra for objects observed at different positions and/or with different orientations. The software used for the spectral extraction is written by one of us (Chen et al. 2005, Paper I). Paper I presents the design and performance of our data reduction software. We detail our reduction steps below.

[1]Information about the observations can be gleaned directly from the STScI WWW pages linked to the program ID.

### 2.2.1. `CALACS` *pipeline and image combination*

We begin with the output from the STScI data pipeline, `CALACS`, which does basic processing of the individual 2D frames. All data have first order bias subtraction, dark subtraction, and bad pixel masking applied. Direct images are then corrected for the flat-field response. Since the flat-field response is a function of wavelength for each pixel and so depends on the location of sources in the dispersed data, the grism data are not flat-fielded.[2]

We combine the *direct* images using a modified version of the `Multidrizzle` package (Koekemoer et al. 2002). `Multidrizzle` is an implementation of the `Blot/Drizzle` technique (Fruchter & Hook 2002) which provides an automated method for distortion-correcting and combining dithered images. `Multidrizzle` corrects for gain and bias offsets between WFC chips and identifies and removes cosmic rays and cosmetic defects. The quality of the image combination relies on accurately determining the offsets between images. The original program aligns images using the World Coordinate System (WCS) header keywords. Unfortunately, there are times when those WCS values are inaccurate, resulting in a misalignment of the final output drizzled product. We have therefore enhanced `Multidrizzle` with the ability to internally verify and update WCS-calculated offsets using image cross-correlation or point-source matching algorithms. The derived shifts and rotations are determined for the geometrically corrected frames resampled onto a common WCS frame. The absolute astrometry of the final drizzled images were verified using guide stars as well as extragalactic sources from NED. The astrometric uncertainties are dominated by the accuracy of the coordinates of the guide stars located in a field area and differ from field to field with a median value of $\sim 0\farcs2$.

[2]The `aXe` ACS grism reduction code of Pirzkal et al. (2002) uses a data cube constructed from observations through narrow-band filters, interpolated to the wavelengths of extracted pixels, to flat-field grism spectra. This technique reduces pixel-to-pixel scatter within the $6000 - 8500$ Å wavelength regime from 3% to 1%, but shows no improvement beyond 8500 Å due to a lack of long-wavelength ACS narrow-band filters. Since the G800L grism mode remains sensitive to $\approx 10\,000$ Å, we opt to omit flat-fielding during spectral extraction (see Paper I for details).

For the *grism* data, our ability to stack raw ACS frames is limited by the substantial geometric distortion and the extent of the offsets between individual exposures. According to the ACS Instrument Handbook, the plate scale changes by 8% between the two diagonal corners of the field. This discrepancy is less than a pixel for dither offsets smaller than 10 pixels. Therefore, we register distorted ACS grism images that have pointing offsets less than 10 pixels into *substacks*, taking care to mask bad pixels and applying a $5\sigma$ clipping algorithm to remove hot pixels and residual cosmic rays. For fields with larger offsets or varying orientations between exposures, we create multiple substacks. Spectral extraction is usually performed on these substacks, then the final coadd is done for 1-dimensional spectra.

Our spectral extraction software (Paper I) requires a pair of aligned direct and dispersed images in the original post-pipeline format; i.e., each WFC chip image must reside in a separate FITS files with the original ACS distortion. We make use of the `Blot` program, which transforms direct images back to the reference frame of G800L image stack(s). We extract 1D spectra from the substacks. In cases with multiple substacks, the 1D extracted spectra are resampled onto a common grid and weight-averaged to create the final deep spectrum.

### 2.2.2. *The Catalog*

We generate object catalogs from the stacked direct image using `SExtractor` (Bertin & Arnouts 1996), applying a $1.5\sigma$ per pixel detection threshold and 8 pixel minimum area requirement. Table 2 presents an example of the catalog produced from our imaging dataset; *the full catalog of emission line galaxies is produced in the on-line version of this paper*. Below we detail some of the listed parameters:

- *Equatorial coordinates* are the barycenter position of a source, that were measured in a WCS-corrected direct image (see § 2.2.1).
- *Magnitudes* are measured in Kron-like AUTO magnitudes and transformed to the Vega photometric system using following zero-points: 26.398 for F606W, 25.256 for F775W, 25.501 for F814W, and 24.326 for F850LP (Pavlovsky 2004).

- *a,b* are the major and minor axis lengths of the fitted ellipse (in units of the 0.″05 ACS/WFC pixels).
- $\theta$ is the position angle of the major axis with respect to the dispersion direction.
- *Concentration*, the Abraham et al. (1996) concentration parameter, is the ratio between the flux in the central 30% of the pixels as compared to the total flux.
- *Asymmetry*, the Abraham et al. (1996) point-asymmetry index, is the absolute sum of the differences between point symmetric pixels divided by the total flux.

#### *2.2.3. 1-D spectral extraction and calibration*

The extraction and calibration of the 1D spectra was carried out with custom software developed by Hsiao-Wen Chen and described in detail in Paper I. We briefly describe the methodology here; the interested reader is directed to Paper I for details.

We first align sources in the direct image (position $x_i, y_i$) with the corresponding position of their zeroth orders in the dispersed image ($x_i^0, y_i^0$), adopting the empirically-derived transformation:

$$\begin{aligned} x_s^0 &= -122.1591 + 1.00442 \cdot x_i - 0.00395 \cdot y_i; \\ y_s^0 &= 3.6392 - 0.00014 \cdot x_i + 1.00088 \cdot y_i \end{aligned} \tag{1}$$

for WFC Chip 1, and

$$\begin{aligned} x_s^0 &= -115.2942 + 1.00444 \cdot x_i - 0.00352 \cdot y_i; \\ y_s^0 &= 2.5025 - 0.00028 \cdot x_i + 1.00068 \cdot y_i \end{aligned} \tag{2}$$

for WFC Chip 2. The extraction region of the spectrum was then computed using transformations derived as part of the calibration program. Using the object brightness distribution inside its segmentation map on the direct image, the corresponding 2D spectra were modeled and overlapping spectra were de-blended via iterative, multiple-profile fitting procedure for all spectra in a frame simultaneously. For objects close to the edges of the dispersed images, only partial spectra were extracted. For faint sources, only first order light is considered; for bright sources, we improve the signal by including higher orders. The rms accuracy of the wavelength calibration for G800L is approximately 7Å (Pasquali et al. 2002). We flux calibrate the extracted spectra using calibration curves derived by Pirzkal et al. (2002) from observations of white dwarfs and Wolf-Rayet stars. The accuracy of the spectrophotometry is limited by uncertainties in the wavelength calibration, the various detector flat-field effects, the object deblending, and variations in the quantum efficiency within individual pixels. We estimate that the absolute flux calibration is accurate to approximately 5% from 5000 Å to 9000 Å.

Spectra were also extracted in a parallel effort using the `aXe` software developed at ST-ECF (Pirzkal et al. 2002). The `aXe` software follows a similar strategy to our code, except it does not perform any deblending due to higher orders from bright objects. Spectra are extracted in weighted boxes, with flat-fielding performed based on observations through narrow-band filters, interpolated to the wavelengths of the extracted pixels. Flux calibration uses the same calibration curves as used by us. The overall results of the extraction and analysis using the `aXe` and our software were similar, except in cases of overlapping spectra where the de-blending included in our code produces significantly cleaner extractions.

## 3. Redshift Identifications

We next cross-correlate the extracted, 1D spectra with a set of stellar and galactic spectral templates in order to deduce an approximate spectral type and redshift for each source. Sources were divided into four groups: Galactic stars, emission-line galaxies (ELGs), early-type galaxies, and galaxies with a Ly$\alpha$ break at $4 < z < 7$. In this paper we present analysis of only the ELGs. Emission-line fluxes and equivalent widths were measured using Gaussian fits to the line and polynomial fitting of the underlying continuum, performed using the ESO-MIDAS `Alice` package. Fig. 2 presents direct images and spectra of a sample of 6 ELGs from this survey. Galaxies were selected to illustrate the range of data quality. Tables 2 and 3 contain the catalog of imaging and spectroscopic properties of the ELGs detected in our fields[3].

[3]The complete version of these tables are in the electronic edition of the Journal. The printed edition contains only a sample.

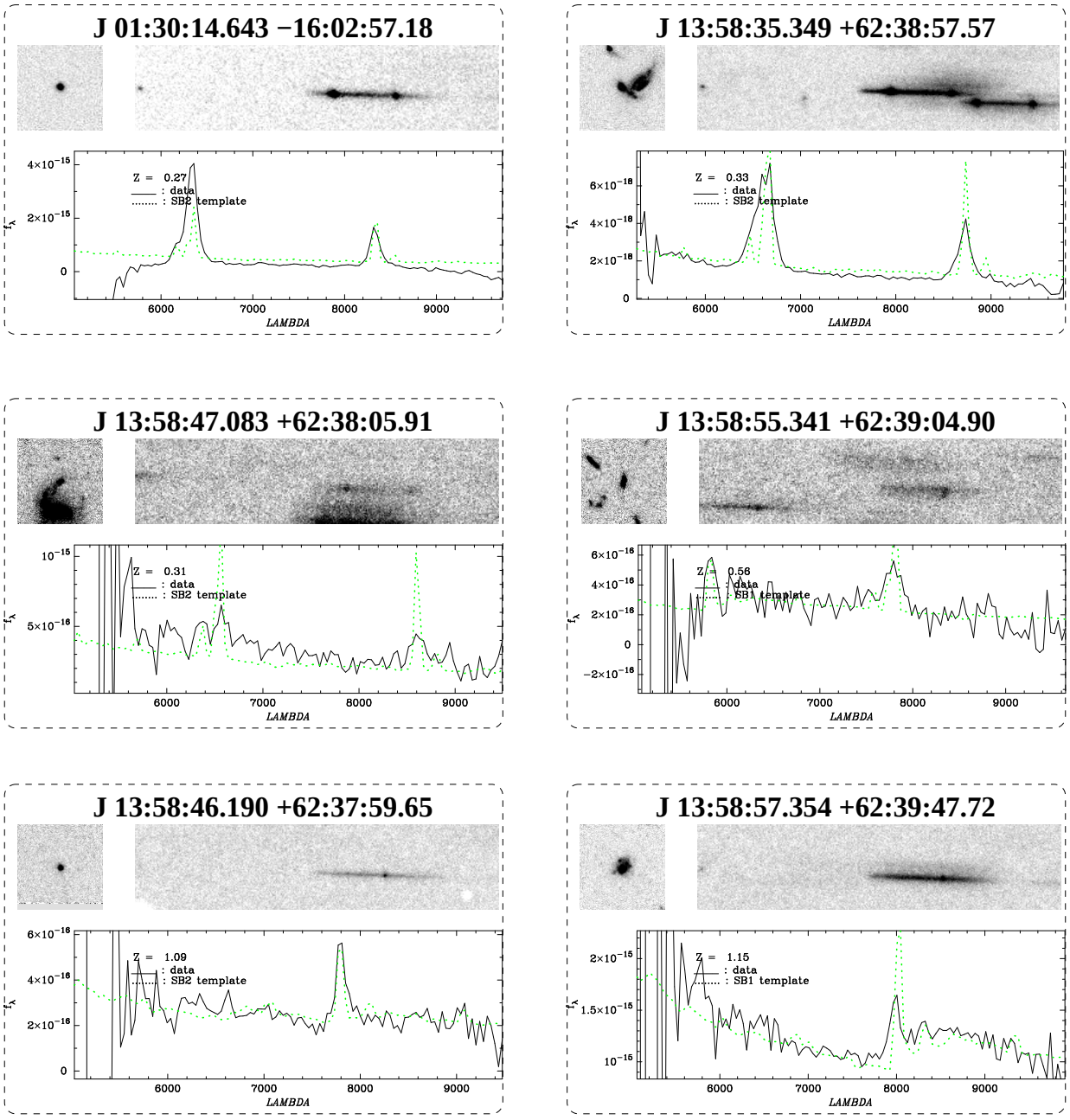


Fig. 2.— Typical emission-line galaxies detected from the ACS Grism Parallel Survey, showing direct images, dispersed images, and extracted 1D spectra. All spectra are shown over observed wavelength range in flux units of erg $s^{-1}$ $cm^{-2}$ $Å^{-1}$. The dotted lines indicate the best-fitting spectral template. Data are sorted by the reliability of their line identifications: the top row shows example of robust, class 'a' redshift identifications, the middle row shows examples of likely, class 'b' redshift identifications, and the bottom row shows less secure, class 'c' redshift identifications. The postage stamp images are 5″ on a side, oriented as per the original data.

### 3.1. The identification of emission lines

Although $\sim 80\%$ of objects with visible emission lines were successfully classified with the cross correlation technique, the accuracy of the redshift determination was low and required visual verification. We compared the ACS spectra to star-forming galaxy templates from Kinney et al. (1996) smoothed to the grism resolution. To convince ourselves that any detected emission line was real, we eliminated all possible false signals (e.g., zero order images, persistent images, cosmic rays, etc.). For final spectral classification, three criteria were used: identified emission line(s), morphology of the emission line(s), and the continuum spectral energy distribution (SED).

To be specific, three major emission features could be present at our observed wavelength range: H$\alpha$ blended with [N II] $\lambda\lambda$6548,6584 (for galaxies at $z < 0.5$), the unresolved [O III] $\lambda\lambda$4959,5007 doublet + H$\beta$ ($0.5 < z < 1.0$), and [O II] $\lambda$3727 ($0.6 < z < 1.7$)[4]. Many sources show multiple emission lines, allowing unambiguous redshift identifications. We note that since the ratio of [O III] $\lambda\lambda$4959,5007 flux to both H$\alpha$ and [O II] $\lambda$3727 flux varies significantly in both the local universe (Terlevich et al. 1991; Kennicutt 1992; Izotov et al. 1994) and at high redshift (e.g., Kobulnicky et al. 1999; Teplitz et al. 2000; Pettini et al. 2001), line flux ratios do not provide a strong redshift indicator.

Galaxies with only a single emission line require more attention. We assume that isolated emission lines are either H$\alpha$ or [O II] $\lambda$3727. Since the [O II]:[O III] ratio can vary from 0.1 to 10, and the [O III]:H$\alpha$ ratio can vary from 0.33 to 1 (Kennicutt 1992), the non-detection of [O III] in an H$\alpha$- or [O II]-emitting galaxy is possible. We choose between H$\alpha$ and [O II] based on the relative position and strength of the line, the continuum SED, as well as the brightness and morphology of the host galaxy in the direct image. For example, a single emission line at wavelengths shortward of 7800 Å that would imply either an H$\alpha$-emitter at a low redshift ($z < 0.2$) or an [O II] emitter at moderate redshift ($z \lesssim 1$). An H$\alpha$-emitter might be expected to appear noticeably larger and brighter in the direct image, possibly showing resolved structure. Since the space density of low-redshift, star-forming compact dwarf galaxies is low, a single, red emission line in a faint galaxy (with a blue rising continuum at shorter wavelength) is most likely [O II] unless there is evidence to the contrary.

Line morphology can also provide a useful redshift diagnostic. At our spectral resolution, the [O III] line is generally asymmetric due to blending with H$\beta$, allowing us to secure line identifications based on the line morphology. On the other hand, [N II] $\lambda\lambda$6548,6584 are not resolved from H$\alpha$ at our resolution, particularly at the low redshifts at which these lines are observed. Some of the compact low-redshift sources, however, reveal the noticeable [S II] $\lambda\lambda$6716,6731 doublet.

We assign a quality (reliability) flag to all redshift estimations based on the number of detected emission lines and significance of their identifications. Quality flag 'a' indicates that there are two or more emission lines identified and that the [O III]+H$\beta$ blend shows a clear asymmetry; this flag indicates that the redshift is secure. A value of 'b' is assigned to galaxies for which there is a strong reason for the assignment. Specifically, such a quality assignment implies we observe multiple emission lines but doubts remain as to their identifications. Quality flag 'c' indicates even greater uncertainty in the redshift identification, typically indicating that only one line has been detected. A non-detection of the second line can be due to several reasons: the most common circumstance is that the galaxy is either at $z < 0.2$ or at $z > 0.8$, and [O III] is in a region of poor spectroscopic sensitivity ($\lambda < 6000$ Å or $\lambda > 9000$ Å). In a few cases, the spectral range is truncated since the galaxy lies near the edge of the field of view.

### 3.2. Comparison with Keck spectroscopy

To test the accuracy of the redshifts and study potentially-interesting faint sources, on UT 2004 March 19 we obtained spectroscopy of two slitmasks targeting ACS-selected galaxies (field J 10:03+29:06) with the Low Resolution Imager and Spectrograph (LRIS; Oke et al. 1995) on the Keck I telescope. These observations were obtained in non-photometric conditions and integration times totaled one hour per slitmask, split into three dithered 1200 s exposures. LRIS is a dual-beam spectrograph: we

[4]Galaxies with Ly$\alpha$ emission at $z > 4$ are not considered here.

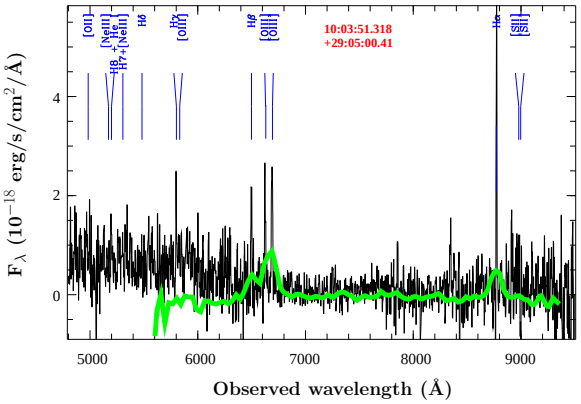


Fig. 3.— Keck/LRIS spectrum (thin line) of one of the ELGs discovered in this survey, overlaid on the ACS grism discovery spectrum (thick grey line). Both LRIS and ACS spectra produced similar redshift determinations, within the expected range considering the $\sim$ 25 times lower spectral resolution of the ACS grism data.

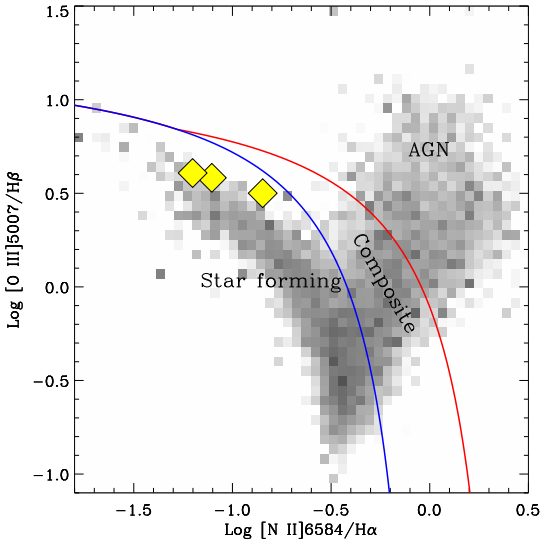


Fig. 4.— The location of three ELGs (diamonds) based on the Keck/LRIS spectra in the BPT line-ratio diagram from Brinchmann et al. (2004). Two lines shows the empiric classification of the ELGs by activity type.

used the D680 beam-splitter, the 300 lines mm$^{-1}$ grism ($\lambda_{\rm blaze}$ = 5000 Å; $\Delta\lambda_{\rm FWHM}$ = 9.0 Å) on the blue arm, and the 400 lines mm$^{-1}$ grating ($\lambda_{\rm blaze}$ = 8500 Å; $\Delta\lambda_{\rm FWHM}$ = 6.4 Å) on the red arm. Data were processed using standard techniques. Because the night was not photometric, we used archival sensitivity functions dating from March 2002 for relative flux calibration.

Unfortunately due to poor weather conditions, we were unable to study the more extreme, faint sources identified from ACS. However, the LRIS data proved quite useful for verifying the accuracy of the ACS-derived redshifts. A total of 11 ACS-selected ELGs were observed, out of which one was of quality 'a', five were of quality 'b', and five were of quality 'c'. In all cases, the ACS and Keck redshifts were consistent. The mean redshift difference is negligible, $\langle z_{\rm ACS} - z_{\rm Keck} \rangle = -0.01 \pm 0.02$. Fig. 3 presents both the ACS and the Keck spectra of one of the sources, J 10:03:51.318+29:05:00.41, at redshift $z$ = 0.337. Note that the H$\beta$/[O III] complex is barely resolved by ACS, but is well-resolved by Keck.

Artificial object tests and comparison of our redshift estimations with ones measured using the higher spectral resolution Keck/LRIS spectra indicate that manual inspection correctly finds the redshifts for over 95% of the spectra.

The Keck/LRIS spectra confirms the high efficiency of the ACS grism selection method, which yields a high fraction of strong-lined galaxies. Namely, 7 out of 11 observed ELGs (64%) have EW([O III] $\lambda$5007)> 100 Å. Such galaxies tend to be either star-burst galaxies with little extinction, or AGN with high-excitation spectra. The general way to classify the ELGs by activity type (AGN versus starburst) is based on the emission line ratios (Baldwin et al. 1981, hereafter BPT). We classify three of these strong-lined sources as star-forming galaxies based on their [O III] $\lambda$5007/H$\beta$ versus N II $\lambda$6584/H$\alpha$ line-ratio, shown in Fig. 4. For the remaining galaxies, comparison of their [O III] $\lambda$5007/H$\beta$ ratio with their [O II] $\lambda$3727/[O III] $\lambda$5007 ratio, immeasurably weak [Ne III] $\lambda$3826 line, and narrow emission lines confirm that they are also starburst systems.

## 4. Results

### 4.1. Areal coverage and depth

Based on the analysis of eleven fields, we detect 601 galaxies revealing significant emission features, corresponding to a surface density of $\sim$ 5 ELGs arcmin$^{-2}$. Among them we identify

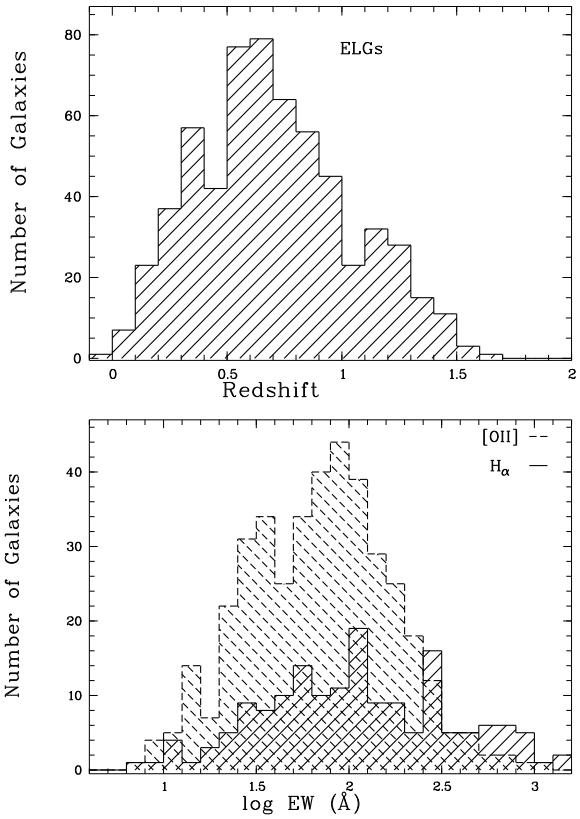


Fig. 5.— Redshift distribution (top) and observed equivalent width distribution (bottom) for detected ELGs.

166 galaxies with H$\alpha$ emission, 406 galaxies with [O III]+H$\beta$ emission, and 401 galaxies with [O II] emission. Our survey is most sensitive to emission line sources with angular sizes (in the dispersion direction) of less than 1 arcsec and with broadband magnitudes of F814W $\lesssim$ 26 mag. Fig. 5 shows the redshift and equivalent width distribution for the survey and Fig. 6 plots line flux fluxes against F814W magnitude. Our ELG sample has a median redshift of 0.66. At low redshifts, the fall off in H$\alpha$-emitting galaxies is attributed to the small volume covered by survey. At high redshifts, the number of sources falls as the sensitivity drops and our primary rest-frame optical features enter the near-infrared. There is also some plunge in the number of detected single-line galaxies at $0.4 < z < 0.5$ and $1.0 < z < 1.1$, when second H$\alpha$ and [O III] lines move into the near-IR.

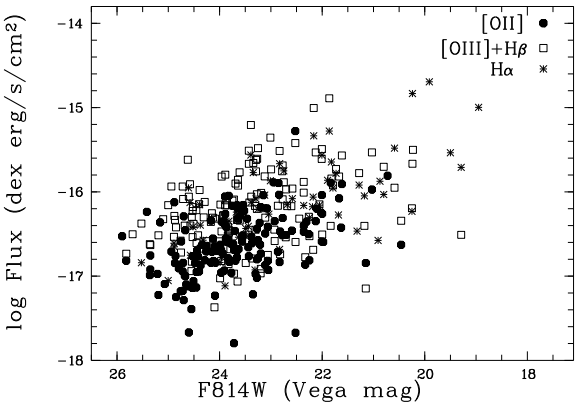


Fig. 6.— Emission line fluxes versus F814W magnitude. The symbols indicate different emission features: asterisks indicate H$\alpha$ emission, empty squares indicate [O III] emission, and filled circles indicate [O II] emission. The ACS grism survey identifies galaxies to very faint continuum brightness levels.

### 4.2. The emission-line luminosity

The distribution of the emission-line luminosities, ignoring dust extinction corrections, is presented in Fig. 7. The median H$\alpha$ line luminosity of galaxies in our survey is $2.7 \times 10^{40}\, h_{70}^{-2}$ ergs s$^{-1}$; this is 26 times fainter than characteristic luminosity $L^*_{H\alpha} = 7.1 \times 10^{41}\, h_{70}^{-2}$ ergs s$^{-1}$ derived from surveys of the local universe (e.g., Gallego et al. 1995; Tresse & Maddox 1998), and 132 times fainter than $L^*_{H\alpha} = 3.6 \times 10^{42}\, h_{70}^{-2}$ ergs s$^{-1}$ at $z = 1.3$ (Yan et al. 1999). The median [O II] line luminosity is $8.5 \times 10^{40}\, h_{70}^{-2}$ ergs s$^{-1}$. The median [O II] luminosity for the $z > 0.6$ sample is two times fainter than the local $L^*_{[OII]} = 1.7 \times 10^{41}\, h_{70}^{-2}$ ergs s$^{-1}$ derived by the Universidad Complutense de Madrid survey (UCM; Gallego et al. 2002). The median [O III]+H$\beta$ line-blend luminosity can be compared with single [O III] $\lambda$5007 line luminosity $L^*_{[OIII]5007} = 1 \times 10^{42}\, h_{70}^{-2}$ ergs s$^{-1}$ calculated by Hippelein et al. (2003) for galaxies in the redshift range $0.62 < z < 0.65$. Our cumulative [O III]+H$\beta$ value of $L^*_{[OIII]+H\beta} = 7.4 \times 10^{40}\, h_{70}^{-2}$ ergs s$^{-1}$ is again 14 times fainter. Our survey is clearly reaching down to the faint end of the emission-line luminosity functions. Our sample selects star-forming galaxies over a wide range of luminosity, from faint emission-line galaxies at

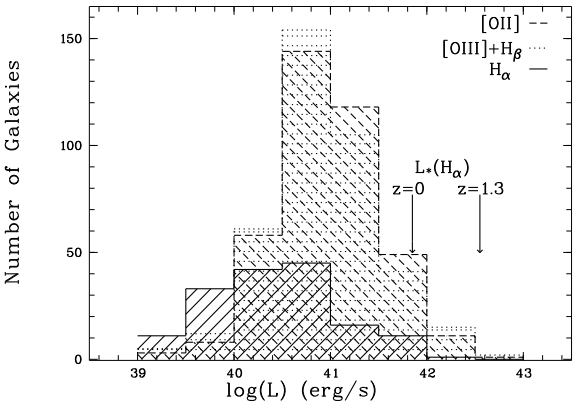


Fig. 7.— Histogram of H$\alpha$ (solid line), [O III]+H$\beta$ (dotted line) and [O II] (dashed line) luminosities in the ACS Grism Parallel Survey. Vertical lines indicate the characteristic H$\alpha$ line luminosity for the local universe (Gallego et al.1995) and at $z = 1.3$ (Yan et al.1999).

low redshifts to luminous L$^*$ galaxies at high redshifts.

### 4.3. The emission-line luminosity and star formation rate

H$\alpha$ emission is a classic indicator of star formation because it traces the ionizing flux from hot stars. Assuming Case B recombination and a Salpeter initial mass function over the mass range $0.1 < M/M_\odot < 100$, we adopt the calibrations of Kennicutt (1998) between star formation rate (SFR) and H$\alpha$ luminosity:

$$\mathrm{SFR_{H\alpha}}\,(\mathcal{M}_\odot\,\mathrm{yr}^{-1}) = 7.9\times10^{-42}\cdot L_{\mathrm{H\alpha}}\,(\mathrm{erg\,s}^{-1}). \quad (3)$$

Assuming the average H$\alpha$ to [O II] flux ratio of 0.45, the Kennicutt (1998) relation implies

$$\mathrm{SFR_{[OII]}}\,(\mathcal{M}_\odot\,\mathrm{yr}^{-1}) = 1.4\times10^{-41}\cdot L_{\mathrm{[OII]}}\,(\mathrm{erg\,s}^{-1}), \quad (4)$$

subject to the considerable scatter in this flux ratio found in surveys of local galaxies, likely associated with variations in the metallicity and star formation histories of individual galaxies. Furthermore, we note that since no extinction corrections have been applied, the derived luminosities and star formation rates should be considered lower limits.

While H$\beta$ line is also a good tracer of star formation in galaxies (e.g., Kennicutt 1983), it is blended with the [O III] $\lambda\lambda$4959,5007 doublet in our low-resolution spectra. The strength of the oxygen lines, however, also correlate with the formation rate of massive stars, and may be used as a proxy for the SFR in cases where [O II] and H$\alpha$ are unavailable (e.g., Teplitz et al. 2000; Hippelein et al. 2003). Due to its high ionization level, the luminosity of [O III] depends strongly upon the temperature of the ionized gas, which in turn depends upon the metallicity of the galaxy. In order to convert the [O III]+H$\beta$ line blend into a star formation rate, an averaged intensity ratio between these lines and H$\alpha$ must therefore be established. Having detected and measured a large number of ELGs, revealing either the [O III] and H$\alpha$ or the [O III] and [O II] line pairs, we can test the correlation between [O III] luminosity and SFR with the understanding that the analysis is inherently limited by the unknown properties of the galaxies.

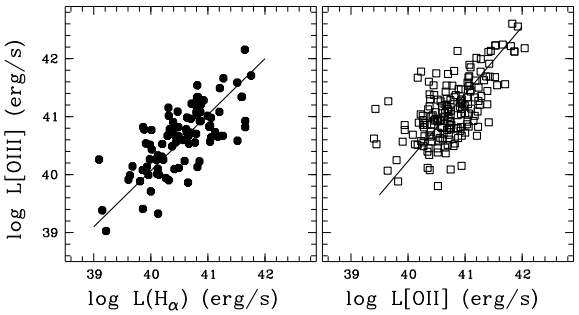


Fig. 8.— [O III]+H$\beta$ line-blend luminosities plotted against H$\alpha$ and [O II] luminosities for the ACS Grism Parallel Survey. Lines show the best fit correlation derived from orthogonal regression. While the scatter is considerable, a correlation is obvious.

Fig. 8 compares the [O II], [O III], and H$\alpha$ luminosities. Assuming the average H$\alpha$:[O II] ratio of $\sim$ 0.6, the median [O III]:H$\alpha$ ratio of $\approx$ 1.3 we derive from 127 ACS grism ELGs at $z \lesssim 0.6$ is in agreement with the median [O III]:[O II] $\approx$ 2.2 ratio we derive from 245 ACS grism ELGs at $0.5 \lesssim z \lesssim 1.0$. Using these ratios and equations (3) and (4), we derive

$$\mathrm{SFR_{[OIII]+H\beta}}\,(\mathcal{M}_\odot\,\mathrm{yr}^{-1}) \simeq 6\times10^{-42}\cdot L_{\mathrm{[OIII]+H\beta}}\,(\mathrm{erg\,s}^{-1}). \quad (5)$$

We expect this SFR indicator to have the largest scatter of the three considered; consequently, we only use it for the 47 galaxies in our sample (less than 8%) which reveal only a single [O III] line

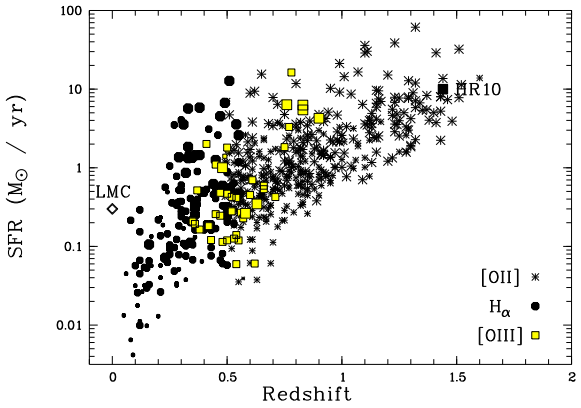


Fig. 9.— SFR derived from H$\alpha$ (circles), [O III] (squares) and [O II] luminosities (asterisks). Size of the symbol is proportional to the object absolute broad-band magnitude (in F814W or F775W). The current H$\alpha$-derived SFR for the Large Magellanic Cloud (LMC) is indicated by an open diamond (Kennicutt, Tamblyn & Congdon 1994). A filled square illustrates the [O II]-derived SFR of the dusty, red starburst galaxy HR10 (Dey et al. 1999).

and lack other emission lines.

We plot the derived star formation rates[5] against redshift in Fig. 9. At each redshift, our dynamic range in observed SFR is approximately 1.5 orders of magnitude, and we see the expected bias of finding higher SFRs at higher redshifts. The majority of the surveyed H$\alpha$ emitters are mildly star-forming, local galaxies. The median SFR of H$\alpha$-emitters in our survey is $0.2\,\mathcal{M}_\odot\,\mathrm{yr}^{-1}$. After correcting for [N II] $\lambda\lambda$6548,6584 contamination using the average [N II]:H$\alpha$ ratio of 0.3 derived by Gallego et al. (1997) from a local sample of galaxies, this rate is reduced to $\sim 0.1\,\mathcal{M}_\odot\,\mathrm{yr}^{-1}$. This SFR is typical of local dwarf galaxies: e.g., the median SFRs of the local blue compact galaxies is about $0.3\,\mathcal{M}_\odot\,\mathrm{yr}^{-1}$ (Hopkins et al. 2002), and the H$\alpha$-derived SFR for the nearest irregular galaxies, LMC and SMC are, respectively, 0.26 and $0.046\,\mathcal{M}_\odot\,\mathrm{yr}^{-1}$ (Kennicutt et al. 1994).

Using equation (4), we determine that the SFR of [O II]-emitters in our survey span nearly 3 orders of magnitude, from approximately a few times $10^{-2}$ to several times $10^{1}\,\mathcal{M}_\odot\,\mathrm{yr}^{-1}$, with a median SFR of about $1.2\,\mathcal{M}_\odot\,\mathrm{yr}^{-1}$. Our survey is sensitive enough to detect objects with SFRs as low as $1\,\mathcal{M}_\odot\,\mathrm{yr}^{-1}$ up to $z \approx 1.2$. At higher-redshift the ACS grism survey reaches typical starburst galaxies with SFRs of $20 - 60\,\mathcal{M}_\odot\,\mathrm{yr}^{-1}$ (e.g., Glazebrook et al. 1999; Savaglio et al. 2004). Even a distant analog of the ULIRG population, such as ERO J164502+4626.4 — also known as HR10 ($\mathrm{SFR}_{[\mathrm{OII}]} \approx 10\,\mathcal{M}_\odot\,\mathrm{yr}^{-1}$; Dey et al. 1999) — can be among our high-redshift sample.

A major concern remains the large uncertainty in SFRs derived from oxygen fluxes. It has previously been noted in surveys of the local universe that the [O II]:H$\alpha$ ratio correlates with total galaxy luminosity, such that brighter galaxies have lower [O II]:H$\alpha$ ratios (e.g. Jansen et al. 2001; Tresse et al. 2002). This correlation is thought to be related to metallicity. The variation in the [O III]:H$\alpha$ ratio is even more dependent on metallicity, as well as on the effective temperature of the gas and the ionization parameter (Kennicutt et al. 2000), so we proceed with this caution in mind. We note, however, that the [O II] and [O III] measurements of the SFR do not show a large discontinuity with the H$\alpha$ measurements at the transitional region of $z \approx 0.5$ (Fig. 9); apparently, the SFR determinations from oxygen lines are not completely wrong.

A rough estimate of the number density of star-forming galaxies can be made using galaxies detected at $0.3 \leq z \leq 1.3$, such that their H$\alpha$ and [O II] lines are in efficient regions of the sensitivity curve. The total angular area of the eleven selected fields is 121 arcmin$^2$, corresponding to a co-moving volume of $1.13 \times 10^5\,h_{70}^{-3}$ Mpc$^3$. We detected 506 ELGs in this redshift interval, giving a co-moving number density of $4.5 \times 10^{-3}\,h_{70}^{-3}$ Mpc$^{-3}$. The co-moving number density of [O II]-emitters in our survey at $0.5 < z < 1.3$ is $\sim 3.8 \times 10^{-3}\,h_{70}^{-3}$ Mpc$^{-3}$. This density is about 7 times higher than that detected by the STIS parallels (Teplitz et al. 2003) at $0.5 < z < 1.2$. The NICMOS parallel survey (McCarthy et al. 1999) detected 33 H$\alpha$ emitters at $0.7 < z < 1.9$ in the co-moving volume of $0.78 \times 10^5\,h_{70}^{-3}$ Mpc$^3$. Thus the co-moving number density of ELGs averaged over their volume is $\sim 0.4 \times 10^{-3}\,h_{70}^{-3}$ Mpc$^{-3}$. As Yan et al. (1999) and Teplitz et al. (2003) point out, their surveys

[5]Note that since our fluxes are not corrected for any absorption effect, the values we present are a low limit to the true SFRs.

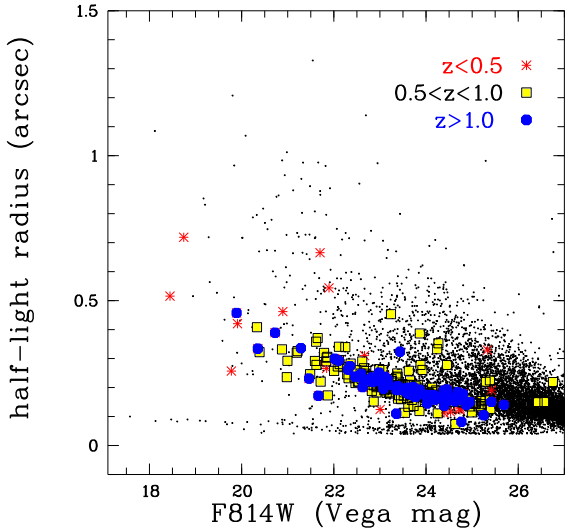


Fig. 10.— Half-light radius versus total magnitude for three ELG redshift bins (large symbols, as indicated). For comparison, all sources in our direct images are plotted as small dots. The concentration of the ELGs among the objects of small angular size objects is evident.

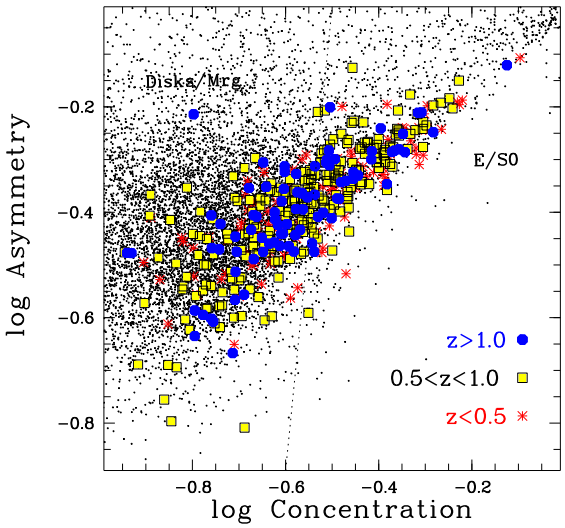


Fig. 11.— The distribution of ELGs on the central concentration − asymmetry ($C-A$) plane, as measured in F775W/F814W images. Large symbols represent ELGs; dots show all sources detected in the direct images. The dotted line is a rough border between disk and bulge dominated galaxies, defined from the visual classification of well-resolved, bright galaxies.

probed starburst galaxies from the upper end of the luminosity function. Our data set is able to detect much fainter emission lines and measure the co-moving star formation density at $z < 1.6$ to better completeness levels. On the other hand, the redshifts measurements based on the ACS/WFC slitless spectra are subject to larger uncertainties due to the lower spectral resolution of ACS as compared to STIS and NICMOS[6].

### 4.4. The morphology of the ELGs

The high spatial resolution of the ACS/WFC images enable a detailed study of the morphological properties of ELGs. We defer a detailed study to a future paper and present here plots of basic morphological parameters for the ELG sample, such as half-light radius, concentration, and asymmetry. We analyze F775W/F814W images (observed $I$-band), which correspond to rest-frame $B$-band for the median redshift of our ELG sample, $\langle z \rangle \sim 0.7$. The morphology at this rest-frame wavelength is dominated by star-formation regions. Fig. 10 plots half-light radius against total magnitude for all objects detected in our imaging, with identified ELGs indicated. Because of band-shifting effects and surface brightness dimming, plot symbols are keyed to redshift. As expected, the survey is biased towards obtaining redshifts for compact galaxies.

The morphological classifications of the ELGs galaxies were performed on the basis of both the visual inspection and automatic classification using central concentration ($C$) and rotational asymmetry ($A$) indexes (Abraham et al. 1994; Abraham et al. 1996). As shown by Abraham et al., these parameters are remarkably robust to image degradation resulting from increased line-of-sight distance. Visual classification, however, is more sensitive to peculiar and merging galaxies. The comparison of visual with quantitative morpholog-

[6]The deep, targeted NICMOS survey of the 4.4 arcmin$^2$ Groth-Westphal strip (Hopkins et al. 2000) detected 37 H$\alpha$ emitters at $0.7 < z < 1.8$, corresponding to the co-moving number density of $\sim 7.3\times10^{-3}\, h_{70}^{-3}$ Mpc$^{-3}$. We also expect that the GRAPES ACS grism survey of the Hubble Ultra Deep Field (Pirzkal et al. 2004), with total grism time $\sim 28$ hours, will reveal a much larger number density of emission-line galaxies within the same redshift range as our survey.

ical classifications show good agreement in $\sim 70\%$ of galaxies brighter than F814W$= 22$. For fainter galaxies, it is not trivial to distinguish E from S0 galaxies, and Sb or Sc spirals from Sd and Irr galaxies. Therefore, based on the visual calibration of well-resolved, bright galaxies, we distinguish here two classes of objects: disk-dominated and bulge-dominated galaxies.

The distribution of the entire imaging data set on the $C - A$ plane is shown in Fig. 11, revealing the variety of their morphological types. The fraction of disk versus bulge dominated objects in our sample is almost equal. The $C - A$ plot is also characterized by a correlated distribution of the ELGs, which can be well approximated by $\log A = (0.53 \pm 0.03) \cdot \log C - (0.08 \pm 0.02)$. The small fraction of ELGs among highly asymmetric galaxies might be explained by our bias towards galaxies of small angular size. The less concentrated disk-like systems show a larger spread in asymmetry, with many of them resembling interacting, merging, and peculiar systems.

### 4.5. ACS simulations and completeness tests

There are several aspects of the data which negatively impact our ability to identify genuine spectral features. Since we are observing in slitless mode, each object produces zero, first and second order spectra. The first order spectra contain the most useful data; the second order is profitable for bright objects; zero, negative and higher ($> 2^{\rm nd}$) orders are sources of confusion. The zero-order images can can be mistaken for emission features, particularly when they fall on the first order continua of other objects. The zero-order images are slightly dispersed ($\sim 650$ Å pix$^{-1}$) and often appear bimodal for point sources. The displacement between the zero order images and the center of the corresponding direct image (near the start of the first order spectrum) is $\sim 5\farcs5$, or $\sim 110$ pix, and generally can be identified by matching them with either the first order spectra or with an object in the direct image. There is a small portion of the detector, however, for which zero-order images can appear *without* either first order spectra or images in the direct frame. In addition to the confusion caused by spectral orders, there are artifacts associated with defective pixels and cosmic rays.

We performed completeness tests using artificial object trials with the `SLIM` program (Pirzkal et al. 2001), using a set of template starburst (SB1) galaxy spectra from Kinney et al. (1996). The original `SLIM` configuration parameters were adjusted to correspond to the current best-known ACS/WFC/G800L grism spectral trace and dispersion descriptions. A total of $\sim 600$ pairs of the synthetic direct images and $z = 0.7$ SB1 template spectra were generated with `SLIM` and randomly added to our F814W and G800L data for the J 13:58+62:39 field. The synthetic images used Gaussian brightness profiles with radii $0\farcs1 \leq r \leq 0\farcs5$ and magnitudes in the range $23.0 \lesssim$ F814W $\lesssim 24.5$. Object spectra were extracted using the same method we used for the real objects and the emission-line parameters were measured and compared with input ones.

Objects were considered recovered if they were found in both direct and grism images, the emission lines were detected at the $> 3\sigma$ level, and the measured equivalent widths did not exceed the initial, injected values by 20 Å. Fig. 12 shows the outcome of these completeness tests. These plots reveal strong selection effects are present in our sample of ELGs. More detailed tests, necessary for the calculation of the luminosity function and measurements of co-moving star formation rate, will be discussed in Paper III.

The quality of the flux and wavelength calibration have also been tested on data taken at different epochs and located at different parts of the ACS/WFC detector: we find good agreement. The rms accuracy of redshifts derived from repeat observations is $\sim 0.02$.

### 4.6. Notes on Individual Fields

#### *4.6.1. Field J 13:58+62:39*

This field has the largest total grism exposure time of all the survey fields, and reveals many interesting objects. We identify more than 40 ELGs, including a concentration of galaxies at $z \sim 0.3$.

#### *4.6.2. Field J 12:19+06:49*

This field was parallel to a program aiming at a Virgo cluster galaxy, located in the outer regions of the cluster. We detect a small, low surface brightness spheroidal galaxy at 12:19:10.96, +06:47:54.0 (J2000), which has a bright, compact source at its

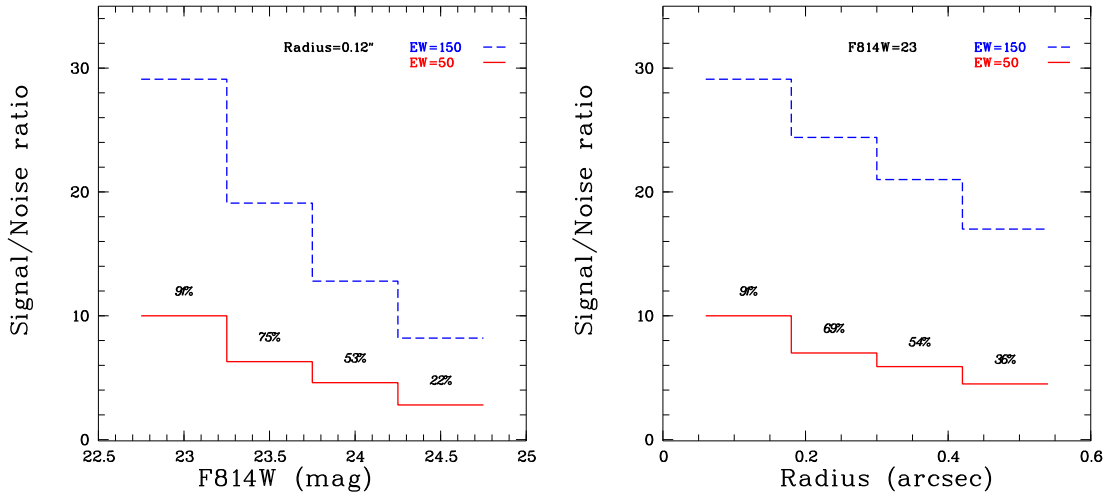


Fig. 12.— Simulated emission line signal-to-noise ratio (S/N), as a function of galaxy magnitude (left) and radius (right). The solid line is the mean S/N of an [O II] emission line with an equivalent width (EW) of 50 Å. The dashed line is same for an [O III] emission-line with EW= 150 Å , corresponding to the SB1 spectral template Kinney et al. (1996) redshifted to $z = 0.7$. The fraction of [O II]-sources detected at $> 3\sigma$ (in percent) are shown in italics.

optical center with blue-excess continuum. However, it is unclear if the central object is associated with the galaxy. Based on the galaxy patchy faint background traced out to galactocentric radii of $\approx 10''$ in both $F775W$ and $F850LP$-band images, the galaxy appears to be an isolated spheroidal galaxy, likely at the distance of the Virgo cluster. At the same time, we could not rule out the possibility that this is a Galactic source (e.g., planetary nebula). No record of this object exists in NED or SIMBAD.

#### *4.6.3. Field J 10:03+29:06*

This field shows a surprisingly large number of ELGs, despite its short total grism exposure time. Eleven emission line galaxies and several candidates high-redshift Ly$\alpha$ emitters were observed with Keck/LRIS, as discussed in §3.2; however, conditions for this ground-based spectroscopy were insufficient for obtaining useful data on any but the brightest galaxies.

#### *4.6.4. Field J 08:06+06:43*

The ACS data for this field is part of the GO program 9405 (P.I. Andrew Fruchter), which targeted the host galaxy of supernova SN 2002LT, associated with gamma-ray burst GRB021211 (Crew et al. 2003). The ACS grism spectrum confirms the presence of an emission line at $\sim$ 7450 Å at the position of the probable host galaxy (J 08:08:59.828, +06:43:37.52), as previously detected in a VLT/FORS2 spectrum by Vreeswijk et al. (2003). This line is likely [O II] $\lambda$3727 at z=1.006. The deep multi-epoch slitless and direct data allow us to detect 88 ELGs in this field.

## 5. Discussion

We present basic data derived from the ACS Grism Parallel Survey. The G800L grism on ACS provides a unique opportunity to survey large volumes of the universe for faint emission lines and at high angular resolution. The small pixel scale of the ACS images and our custom software for deblending object spectra provides us with the unique opportunity to identify faint star-forming regions across vast cosmic epochs. The large dataset afforded by our "random" parallel observations allows us to collect data from much larger area than would be possible in a single GO program.

The ACS Grism Parallel Survey complements

previous and ongoing surveys of [O II], [O III] and H$\alpha$ ELGs. Our faint flux limits allow us to probe deeper into the ELG luminosity function. In this paper we present our methodology for data analysis and the first results from our survey. Our initial survey of 121 square arcminutes detects 601 emission-line galaxies at redshifts $z \leq 1.6$. The line luminosities, equivalent widths and continuum magnitudes suggest that we are seeing galaxies with a broad range of star formation rates, from quiescently star-forming galaxies at low redshifts to bright starburst galaxies at $z > 1$.

The survey is biased towards compact objects with strong emission lines. Such galaxies tend to be either starbursts and/or AGNs. Follow-up high-resolution spectra are necessary in order to classify each ELG by its activity. To date we have obtained follow-up spectra for 11 candidates, all of them found to be starforming ELGs with seven being starbursts (see §3.2). While this subsample is small, we infer that the fraction of AGN in our sample is small and that the inferred emission-line luminosities can be used to estimate the co-moving star formation density at $z \leq 1.6$ at a high confidence level.

The authors also wish to recognize and acknowledge the very significant cultural role and reverence that the summit of Mauna Kea has always had within the indigenous Hawaiian community; we are most fortunate to have the opportunity to conduct observations from this mountain. ID acknowledges the support from NASA HST grant GO-9468. The work of DS was carried out at Jet Propulsion Laboratory, California Institute of Technology, under a contract with NASA.

## REFERENCES

Abraham, R. G., Tanvir, N. R., Santiago, B. X., Ellis, R. S., Glazebrook, K., & van den Bergh, S. 1996, MNRAS, 279, L47

Abraham, R. G., Valdes, F., Yee, H. K. C., & van den Bergh, S. 1994, ApJ, 432, 75

Baldwin, J. A., Phillips, M. M., & Terlevich, R. 1981, PASP, 93, 5

Bertin, E. & Arnouts, S. 1996, A&AS, 117, 393

Brinchmann, J., Charlot, S., White, S. D. M., Tremonti, C., Kauffmann, G., Heckman, T., & Brinkmann, J. 2004, MNRAS, 351, 1151

Chen, H.-W. et al. 2005, ApJ, in preparation

Cimatti, A., Daddi, E., Renzini, A., Cassata, P., Vanzella, E., Pozzetti, L., Cristiani, S., Fontana, A., Rodighiero, G., Mignoli, M., & Zamorani, G. 2004, Nature, 430, 184

Cohen, J. G., Hogg, D. W., Blandford, R., Cowie, L. L., Hu, E., Songaila, A., & Shopbell, P. 2000, ApJ, 538, 29

Cowie, L. L., Songaila, A., & Barger, A. J. 1999, AJ, 118, 603

Cowie, L. L., Songaila, A., Hu, E. M., & Cohen, J. G. 1996, AJ, 112, 839

Crew, G. B., Lamb, D. Q., Ricker, G. R., Atteia, J.-L., et al. 2003, ApJ, 599, 387

Dey, A., Graham, J. R., Ivison, R. J., Smail, I., Wright, G. S., & Liu, M. C. 1999, ApJ, 519, 610

Fruchter, A. S. & Hook, R. N. 2002, PASP, 114, 144

Gallego, J., Garcia-Daba, C. E., Zamorano, J., Aragon-Salamanca, A., & Rego, M. 2002, ApJ, 570, L1

Gallego, J., Zamorano, J., Aragon-Salamanca, A., & Rego, M. 1995, ApJ, 455, L1

Gallego, J., Zamorano, J., Rego, M., & Vitores, A. G. 1997, ApJ, 475, 502

Gardner, J. P. et al. 1998, ApJ, 492, L99

Gavazzi, G. & Scodeggio, M. 1996, A&A, 312, 29

Glazebrook, K., Abraham, R. G., McCarthy, P. J., Savaglio, S., Chen, H., Crampton, D., Murowinski, R., Jørgensen, I., Roth, K., Hook, I., Marzke, R. O., & Carlberg, R. G. 2004, Nature, 430, 181

Glazebrook, K., Blake, C., Economou, F., Lilly, S., & Colless, M. 1999, MNRAS, 306, 843

Gronwall, C., Jangren, A., Salzer, J. J., Werk, J. K., & Ciardullo, R. 2004, AJ, 128, 644

Hippelein, H., Maier, C., Meisenheimer, K., Wolf, C., Fried, J. W., von Kuhlmann, B., Kümmel, M., Phleps, S., & Röser, H.-J. 2003, A&A, 402, 65

Hopkins, A. M., Connolly, A. J., & Szalay, A. S. 2000, AJ, 120, 2843

Hopkins, A. M., Schulte-Ladbeck, R. E., & Drozdovsky, I. O. 2002, AJ, 124, 862

Hu, E. M., Cowie, L. L., & McMahon, R. G. 1998, ApJ, 502, 99

Izotov, Y. I., Thuan, T. X., & Lipovetsky, V. A. 1994, ApJ, 435, 647

Jansen, R. A., Franx, M., & Fabricant, D. 2001, ApJ, 551, 825

Kennicutt, R. 1983, ApJ, 282, 54

Kennicutt, R. C. 1992, ApJ, 388, 310

—. 1998, ARA&A, 36, 189

Kennicutt, R. C., Bresolin, F., French, H., & Martin, P. 2000, ApJ, 537, 589

Kennicutt, R. C., Tamblyn, P., & Congdon, C. E. 1994, ApJ, 435, 22

Kinney, A. L., Calzetti, D., Bohlin, R. C., McQuade, K., Storchi-Bergman, T., & Henrique, R. 1996, ApJ, 467, 38

Kobulnicky, H. A., Kennicutt, R. C., & Pizagno, J. L. 1999, ApJ, 514, 544

Kodaira, K. et al. 2003, PASJ, 55, L17

Kodama, T., Yamada, T., Akiyama, M., Aoki, K., Doi, M., Furusawa, H., Fuse, T., Imanishi, M., Ishida, C., Iye, M., Kajisawa, M., Karoji, H., Kobayashi, N., Komiyama, Y., Kosugi, G., Maeda, Y., Miyazaki, S., Mizumoto, Y., Morokuma, T., Nakata, F., Noumaru, J., Ogasawara, R., Ouchi, M., Sasaki, T., Sekiguchi, K., Shimasaku, K., Simpson, C., Takata, T., Tanaka, I., Ueda, Y., Yasuda, N., & Yoshida, M. 2004, MNRAS, 350, 1005

Koekemoer, A. M., Fruchter, A. S., Hook, R. N., & Hack, W. 2002, in The 2002 HST Calibration Workshop : Hubble after the Installation of the ACS and the NICMOS Cooling System, Ed. by Santiago Arribas, Anton Koekemoer, and Brad Whitmore. Baltimore: STScI, 339

Lilly, S. J., Fevre, O. L., Hammer, F., & Crampton, D. 1996, ApJ, 460, L1

McCarthy, P. J. et al. 1999, ApJ, 520, 548

Pasquali, A., Walsh, J., & Pirzkal, N. 2002, MNRAS, tbd

Pavlovsky, C. e. a. 2004, ACS Data Handbook, Tech. Rep. Version 3.0, Baltimore: STScI

Pettini, M., Shapely, A. E., Steidel, C. C., Cuby, J., Dickinson, M., Moorwood, A. F. M., Adelberger, K. L., & Giavalisco, M. 2001, ApJ, 554, 981

Pirzkal, N., Pasquali, A., Hook, R., Walsh, J., Fosbury, R., Feudling, W., & Albrecht, R. 2002, in ASP Conf. Ser., Vol. 238, 447

Pirzkal, N., Pasquali, A., Hook, R. N., Walsh, J. R., Fosbury, R. A. E., Freudling, W., & Albrecht, R. 2001, in ASP Conf. Ser. 238: Astronomical Data Analysis Software and Systems X, 447

Pirzkal, N., Xu, C., Malhotra, S., Rhoads, J. E., Koekemoer, A. M., Moustakas, L. A., Walsh, J. R., Windhorst, R. A., Daddi, E., Cimatti, A., Ferguson, H. C., Gardner, J. P., Gronwall, C., Haiman, Z., Kümmel, M., Panagia, N., Pasquali, A., Stiavelli, M., di Serego Alighieri, S., Tsvetanov, Z., Vernet, J., & Yan, H. 2004, ApJS, 154, 501

Rhoads, J. E., Malhotra, S., Dey, A., Stern, D., Spinrad, H., & Jannuzi, B. T. 2000, ApJ, 545, L85

Savaglio, S., Glazebrook, K., Abraham, R. G., et al. 2004, ApJ, 602, 51

Stern, D., Yost, S. A., Eckart, M. E., Harrison, F. A., Helfand, D. J., Djorgovski, S. G., Malhotra, S., & Rhoads, J. E. 2005, ApJ, 619, 12

Teplitz, H. I., Collins, N. R., Gardner, J. P., Hill, R. S., Heap, S. R., Lindler, D. J., Rhodes, J., & Woodgate, B. E. 2003, ApJS, 146, 209

Teplitz, H. I. et al. 2000, ApJ, 533, 65

Terlevich, R., Melnick, J., Masegosa, J., Moles, M., & Copetti, M. V. F. 1991, A&AS, 91, 285

Tresse, L. & Maddox, S. J. 1998, ApJ, 495, 691

Tresse, L., Maddox, S. J., Le Fèvre, O., & Cuby, J.-G. 2002, MNRAS, 337, 369

Vreeswijk, P., Fruchter, A., Hjorth, J., & Kouveliotou, C. 2003, GRB Circular Network, 1785, 1

Yan, L., McCarthy, P. J., Freudling, W., Teplitz, H. I., Malumuth, E. M., Weymann, R. J., & Malkan, M. A. 1999, ApJ, 519, L47

This 2-column preprint was prepared with the AAS LaTeX macros v5.2.

TABLE 1
THE ACS GRISM SURVEY FIELDS

| Field | b[a] | G800L #Exp[b] | G800L Time[c] | F814W #Exp[b] | F814W Time[c] | F814W $m(\sigma)$[d] | F775W #Exp[b] | F775W Time[c] | F775W $m(\sigma)$[d] | F850LP #Exp[b] | F850LP Time[c] | F850LP $m(\sigma)$[d] | F606W #Exp[b] | F606W Time[c] | F606W $m(\sigma)$[d] | Prog. |
|---|---|---|---|---|---|---|---|---|---|---|---|---|---|---|---|---|
| J 01 22 − 28 24 | -83 | 25 | 12825 | | | | 5 | 2437 | 29.6 | 5 | 2530 | 28.8 | | | | 9482 |
| J 01 30 − 16 04 | -76 | 41 | 18525 | | | | 11 | 5768 | 30.3 | 8 | 3700 | 29.3 | | | | 9482 |
| J 02 27 − 40 55 | -66 | 26 | 12218 | 13 | 6195 | 30.3 | | | | | | | | | | 9468 |
| J 07 26 + 69 15 | 28 | 22 | 15526 | | | | 6 | 3200 | 29.8 | 6 | 3060 | 29.1 | | | | 9482 |
| J 08 08 + 06 43 | 20 | 22 | 22390 | 24 | 11680 | 30.8 | | | | | | | 39 | 15580 | 30.9 | 9405 |
| J 10 03 + 29 06 | 53 | 27 | 13481 | 17 | 8750 | 30.5 | | | | | | | | | | 9468 |
| J 11 29 − 14 39 | 44 | 26 | 17398 | | | | 2 | 1000 | 29.2 | 19 | 12911 | 30.0 | | | | 9482 |
| J 12 19 + 06 49 | 68 | 25 | 16800 | | | | 20 | 10938 | 30.5 | 15 | 9798 | 29.7 | | | | 9482 |
| J 13 39 + 00 08 | 61 | 27 | 13678 | | | | 8 | 4460 | 29.9 | 8 | 3760 | 29.1 | | | | 9482 |
| J 13 58 + 62 39 | 53 | 42 | 24319 | 18 | 10226 | 30.7 | 4 | | | 2 | 1000 | 29.0 | | | | 9468 |
| J 15 42 − 10 46 | 34 | 43 | 24024 | | | | 21 | 11586 | 30.1 | 20 | 10669 | 29.8 | | | | 9482 |

[a]Galactic latitude, in degrees.

[b]Number of images and spectra.

[c]The total exposure time, in seconds.

[d]The $1\sigma$ sky *rms* magnitude (Vega system), measured in the aperture of $1 \times FWHM$ diameter (0.1 arcsec). In each filter, the number represents the average value for a whole area of the combined frame.

## Table 2
## Imaging Properties of Emission-Line Objects

| Id | RA (h m s) | DEC (d m s) | $F814W$ (mag[a]) | a (pix) | b (pix) | $\theta$ (deg) | Conc. | Asym. |
|---|---|---|---|---|---|---|---|---|
| 410 | 13:58:46.190 | +62:37:59.65 | 23.54±0.01 | 2.3 | 2.1 | -60.8 | 0.484 | 0.615 |
| 411 | 13:58:47.083 | +62:38:05.91 | 23.82±0.05 | 8.1 | 3.2 | 45.4 | 0.302 | 0.341 |
| 412 | 13:58:49.389 | +62:39:05.53 | 22.84±0.01 | 3.6 | 2.4 | -88.4 | 0.430 | 0.521 |
| 413 | 13:58:51.968 | +62:40:49.81 | 24.51±0.03 | 3.0 | 1.6 | 83.5 | 0.249 | 0.430 |
| 414 | 13:58:52.446 | +62:40:02.95 | 25.70±0.06 | 1.5 | 1.3 | -41.5 | 0.421 | 0.492 |
| 415 | 13:58:53.549 | +62:40:27.43 | 24.45±0.02 | 2.3 | 1.7 | 69.3 | 0.398 | 0.548 |
| 416 | 13:58:54.556 | +62:41:02.73 | 23.15±0.01 | 2.0 | 1.8 | -54.1 | 0.592 | 0.708 |
| 417 | 13:58:54.327 | +62:39:50.81 | 23.63±0.01 | 3.0 | 2.3 | -83.0 | 0.321 | 0.466 |
| 418 | 13:58:59.669 | +62:37:51.34 | 23.00±0.01 | 3.5 | 2.5 | -75.5 | 0.492 | 0.570 |
| 419 | 13:59:00.595 | +62:40:39.99 | 24.61±0.03 | 2.8 | 1.6 | -4.3 | 0.411 | 0.462 |
| 420 | 13:58:57.771 | +62:38:09.23 | 22.75±0.01 | 4.7 | 2.7 | 55.0 | 0.394 | 0.512 |
| 421 | 13:59:00.284 | +62:40:14.23 | 23.46±0.01 | 3.2 | 2.0 | -63.2 | 0.402 | 0.574 |
| 422 | 13:58:57.438 | +62:38:21.04 | 24.72±0.02 | 1.8 | 1.6 | -20.3 | 0.341 | 0.539 |
| 423 | 13:58:57.490 | +62:38:38.09 | 22.13±0.01 | 7.2 | 2.8 | -85.9 | 0.350 | 0.494 |
| 424 | 13:58:57.189 | +62:39:08.42 | 23.90±0.02 | 3.2 | 2.1 | -41.4 | 0.289 | 0.445 |

[a]SYNPHOT standard Vega magnitude

Note.—The complete version of this table is in the electronic edition of the Journal. The printed edition contains only a sample.

## Table 3
## Spectroscopic Properties of Emission-Line Objects

| | | $H_\alpha$ | | | | $H_\beta$+[OIII] | | | | [OII] | | | | | |
|---|---|---|---|---|---|---|---|---|---|---|---|---|---|---|---|
| Id | $z$ | Flux | EW | S/N | cont. | Flux | EW | S/N | cont. | Flux | EW | S/N | cont. | R[a] | Comment.[b] |
| 410 | 1.09 | | | | | | | | | 69.9± 9.9 | 251.8±35.6 | 7.1 | 0.3 | b | |
| 411 | 0.31 | 44.9± 5.8 | 141.6±18.3 | 7.7 | 0.3 | 32.7± 8.3 | 61.3±15.6 | 3.9 | 0.5 | | | | | b | HII? |
| 412 | 1.15 | | | | | | | | | 92.4±30.8 | 92.1±30.7 | 3.0 | 0.8 | c | |
| 413 | 0.69 | | | | | 41.7± 5.0 | 338.1±40.6 | 8.3 | 0.1 | 8.7± 2.9 | 48.6±16.2 | 3.0 | 0.1 | b | |
| 414 | 0.71 | | | | | 31.4± 1.2 | 510.8±20.1 | 25.4 | 0.0 | | | | | a | BCG |
| 415 | 0.83 | | | | | 60.7± 3.5 | 363.3±21.1 | 17.2 | 0.1 | 7.4± 2.5 | 34.7±11.6 | 3.0 | 0.3 | c | S |
| 416 | 0.62 | | | | | 64.0±21.3 | 93.6±31.2 | 3.0 | 0.7 | 91.3±30.4 | 113.6±37.9 | 3.0 | 0.8 | c | BCG? |
| 417 | 0.32 | 29.0± 6.1 | 88.4±18.6 | 4.8 | 0.3 | 55.5±14.1 | 109.9±28.0 | 3.9 | 0.5 | | | | | a | |
| 418 | 0.37 | | | | | 184.9±12.4 | 291.5±19.5 | 15.0 | 0.6 | | | | | a | |
| 419 | 0.01 | 111.6± 2.8 | 956.7±23.6 | 40.5 | 0.1 | | | | | | | | | b | BCG? |
| 420 | 0.29 | 177.4±59.1 | 253.9±84.6 | 3.0 | 0.6 | 130.1±43.4 | 132.0±44.0 | 3.0 | 1.0 | | | | | a | |
| 421 | 1.32 | | | | | | | | | 48.0±16.0 | 141.6±47.2 | 3.0 | 0.3 | c | |
| 422 | 0.69 | | | | | 115.7± 3.4 | 1606.3±47.6 | 33.8 | 0.1 | 11.4± 1.6 | 132.4±18.8 | 7.0 | 0.1 | b | BCG |
| 423 | 0.85 | | | | | 293.8±21.7 | 359.2±26.6 | 13.5 | 0.8 | 44.9±15.0 | 29.2± 9.7 | 3.0 | 1.5 | b | |
| 424 | 0.98 | | | | | | | | | 40.7± 5.4 | 158.4±20.9 | 7.6 | 0.3 | b | BCG |

Note.—All observed fluxes are in unites of $10^{-18}$ ergs cm$^{-2}$ s$^{-1}$, and equivalent widths are in Å. Fluxes and equivalenth widths are not corrected to the rest frame and absorption.

[a]Reliability of line identification: 'a'='Good', 'b'='OK', 'c'='Uncertain'

[b]Symbols are as follows: 'BCG'='Blue Compact Galaxy', 'S'='Spiral', 'Ir'='Irregular', 'HII'='HII region', '#c'='# components'.

Note.—The complete version of this table is in the electronic edition of the Journal. The printed edition contains only a sample.